JOURNAL OF GEOPHYSICAL RESEARCH, VOL. 99, NO. C12, PAGES 25,093–25,107, DECEMBER 15, 1994

Geosat-derived sea level and surface current anomalies in the equatorial Pacific during the 1986–1989 El Niño and La Niña

Thierry Delcroix,[1] Jean-Philippe Boulanger,[2] François Masia,[1] and Christophe Menkes[3]

Abstract. Equatorial wave dynamics are essential in most oceanic models for reproducing aspects of the El Niño–Southern Oscillation (ENSO) phenomenon. In this paper, observational evidence of first baroclinic equatorial Kelvin and first symmetric meridional Rossby waves is found in Geosat-derived sea level anomalies (SLA) and surface zonal current anomalies (ZCA) in the equatorial Pacific ocean during the 1986–1987 El Niño and the ensuing 1988–1989 La Niña. This was made possible after extensive quality control and specific processing of the recently improved Geosat geophysical data records pertaining to the 17-day Exact Repeat Mission. In particular, the processing was made so that the Geosat-derived ZCA best fit near-surface zonal currents from three equatorial moorings at 165°E, 140°W, and 110°W. The Geosat-derived SLA and ZCA are decomposed into first baroclinic equatorial Kelvin and gravest Rossby modes. The emphasis is then put on the chronology of the ZCA at the equator where the currents are the most energetic and where Kelvin and first symmetric Rossby waves explain most of the variance in ZCA, in similar proportion. The 1986–1987 El Niño is mostly characterized by a strong downwelling Kelvin wave in December 1986, a series of downwelling Kelvin waves in March–October 1987, and a strong upwelling Rossby wave in March–September 1987. These waves are consistent with wind forcing, and all give rise to notable eastward ZCA for almost an entire year. During the El Niño–La Niña transition period there is the occurrence of two downwelling Rossby waves originating from the eastern Pacific at times of favorable wind forcing. These Rossby waves switch the basin-wide ZCA from eastward to westward, terminating the warm event. Then, the 1988–1989 La Niña shows the generation of a series of upwelling Kelvin waves which are clearly identified in March/April and September/October 1988. These upwelling Kelvin waves are apparently related to the enhancement of the trade wind in the western half of the basin. These waves maintain the basin-wide westward ZCA for more than a year, although the ZCA is slightly reduced by a front of upwelling Rossby waves in phase with the normal seasonal cycle. The Kelvin wave forcing and sign of Kelvin wave contribution versus Rossby wave contribution to ZCA in the western Pacific are discussed, and we conclude that neither pleads in favor of the delayed action oscillator mechanism.

1. Introduction

Climate variability is caused by complex interactions between geophysical fluids and land surfaces. On interannual timescales, efforts to understand these interactions have mostly focused on the irregular El Niño–Southern Oscillation (ENSO) phenomenon, given its huge signature in and over the tropical Pacific and Indian Oceans, together with its possible impact on global atmospheric and oceanic conditions [see *Philander*, 1990]. Being of major importance to the economies of many nations, ENSO generated a large amount of scientific interest and endeavor with, as a background, the idea to get some skill in its prediction. Although successful predictions were made [*Cane et al.*, 1986], they cannot be fully satisfactory without understanding the intrinsic ENSO mechanisms.

From a theoretical point of view the theory of equatorial waves [*Matsuno*, 1966; *Moore*, 1968] appears as an historically important step toward the understanding of El Niño events, and linear models related to this theory were rather successful in reproducing integrated quantities such as sea level [*Busalacchi and O'Brien*, 1981; *Busalacchi and Cane*, 1985]. Moreover, long equatorial waves have remained pivotal components in models coupling the ocean and the atmosphere, thereby generating new ideas on why ENSO occurs [e.g., *Battisti*, 1988]. From an observational point of view the size of the tropical Pacific was a major impediment to the global description of ENSO and to the assessment of the foundation of equatorial waves. Providing an almost synoptic coverage of the tropical Pacific, at short time intervals, the U.S. Geodetic Satellite (Geosat) was instrumental in these goals (see *Arnault and Périgaud* [1992] for a review). More than one decade after the seminal observa-

[1]Groupe Surveillance Trans-Océanique du Pacifique, ORSTOM, Noumea, New Caledonia.
[2]Laboratoire d'Océanographie Dynamique et de Climatologie, ORSTOM, Université Pierre et Marie Curie, Paris.
[3]Universities Space Research Association, Goddard Space Flight Center, Greenbelt, Maryland.

Paper number 94JC02138.
0148-0227/94/94JC-02138$05.00

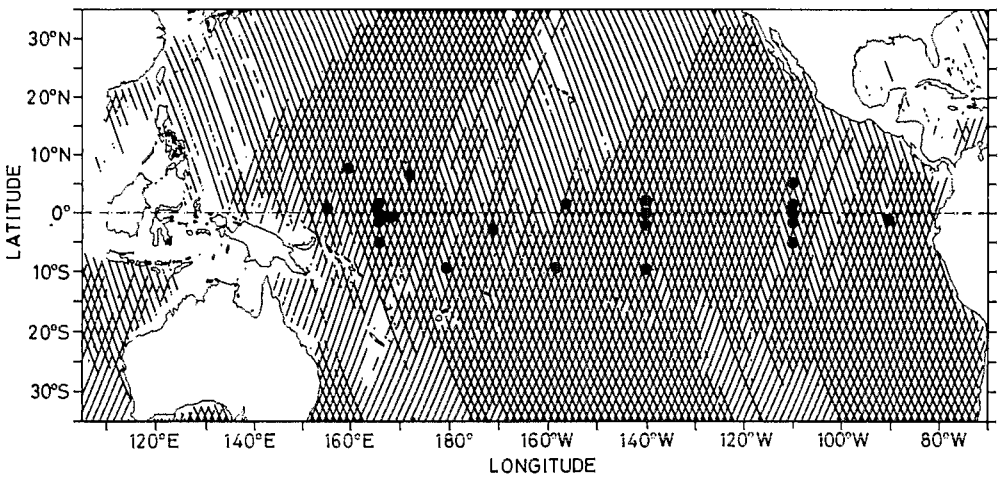

Figure 1. Available ground tracks of the mean Geosat 17-day repeat orbit over the tropical Pacific. The dots denote the locations of in situ comparisons, as detailed in Table 1.

tional work of *Wyrtki* [1975], it is only with the advent of Geosat that equatorial Kelvin and first symmetric Rossby waves were comprehensively evidenced over the whole Pacific basin [*Miller et al.*, 1988; *Delcroix et al.*, 1991].

The present paper is an extension of the work of *Delcroix et al.* [1991] which was based on the first 13 months of the Geosat Exact Repeat Mission, from November 1986 to November 1987. Here we will use an improved version of the Geosat geophysical data record [*Cheney et al.*, 1991], and we will describe and analyze both the 1986–1987 El Niño and the ensuing 1988–1989 La Niña, from November 1986 to February 1989. Also, the emphasis will be put mainly upon the surface zonal current anomalies (ZCA) which are more intrinsically involved than the sea level anomalies (SLA) in equatorial ocean dynamics. Furthermore, the analysis will be done in such a way as to obtain some quantitative information on the actual role and possible origin of equatorial waves. Specifically, the ZCA will be analyzed in terms of orthogonal equatorial waves, assuming that the major contribution to SLA and ZCA is produced by the first baroclinic mode so that the other modes will be ignored. Evidence in support of this is given from models [*Busalacchi and O'Brien*, 1981] and observations [*Gill*, 1982], although the second baroclinic mode is likely to contribute in SLA and ZCA [*Busalacchi and Cane*, 1985; *Bigg and Blundell*, 1989]. Such an approach has already been employed on model results [*Battisti*, 1988; *Wakata and Sarachik*, 1991] and on observational along-track expendable bathythermograph (XBT) data [*Gill and Bigg*, 1985; *Bigg and Blundell*, 1989]. To our knowledge, the basin-wide observation of ZCA during a complete ENSO cycle has been neither described, nor so analyzed previously.

The arrangement of the remainder of the paper is as follows. Section 2 presents the Geosat data and data processing, starting from the raw sea level data to obtaining gridded SLA and ZCA fields. Section 3 details useful supplementary in situ data and their processing. These will be used in section 4 in order to validate the Geosat-derived SLA and ZCA using sea level from 10 island stations situated within 10°N–10°S, 0/500-dbar dynamic height anomalies from 12 moorings in the equatorial belt, and measured ZCA from three equatorial moorings. The description of the standard deviations in Geosat-derived SLA and ZCA over the tropical Pacific is given in section 5, together with first evidence in SLA of first baroclinic equatorial Kelvin and first symmetric Rossby wave propagation during November 1986 to February 1989. In section 6 the respective contributions of equatorial Kelvin and gravest Rossby waves are quantified in ZCA, projecting the SLA and ZCA into meridional modes; details on the projection are found in the appendix. The results indicate that about 70% of the variance in ZCA can be accounted for by equatorial Kelvin and first symmetric Rossby modes within 4°N to 4°S. This is the region where the ZCA are the most energetic and are likely play a crucial role in ENSO cycle. Projection of the zonal wind anomaly forcing into Kelvin and first symmetric Rossby modes is also presented. Focusing only on the equatorial band, section 7 presents a chronology of the ZCA, which are described in terms of Kelvin and first symmetric ($m = 1$) Rossby waves and related to the evolving zonal wind anomaly forcing. A conclusion is given in the last section.

2. Geosat Data and Data Processing

2.1. Geosat-Derived Sea Level Anomaly

The present analysis is derived from the new version of the Geosat geophysical data records (GDR), produced by the National Oceanic and Atmospheric Administration [*Cheney et al.*, 1991]. Following the original GDR [*Cheney et al.*, 1987], this new version uses improved satellite ephemeris and environmental corrections, all of which enhance the overall accuracy of the Geosat data. From the new GDR we have selected data covering the tropical Pacific Ocean (35°S–35°N: 105°E–70°W) from November 8, 1986, to September 26, 1989 (62 cycles). During this period, called the Exact Repeat Mission (ERM), Geosat was in a 72° orbit inclination and its ground tracks repeated every 17 days. At the equator the intertrack distance was about 1.6° longitude and 3 days, although the distance between ascending and descending tracks reduced to 0.8° and 1.5 days (see Figure 1). In the GDR the along-track measurements were averaged every 1 s, resulting in a 6.8-km along-track resolution.

Techniques to retrieve sea surface heights from Geosat altimeter and other measurements are amply documented by

Cheney et al. [1987, 1991]. Here we only outline the corrections we used. Corrections accounting for the effects of solid earth and ocean tides, dry troposphere, ionosphere, inverted barometer, and electromagnetic bias were similar to the ones given in the original GDR. Besides, unlike the original GDR, the new tropospheric water vapor correction was derived from measurements made by the TIROS operational vertical sounder (TOVS) before July 1987 [*Emery et al.*, 1990] and by the special sensor microwave/imager (SSM/I) from July 1987 [*Wentz*, 1989]. Moreover, the new orbit was calculated from the ephemeris computed by *Haines et al.* [1990] which is based on the geopotential Goddard Earth Model (GEM)-T2 of *Marsh et al.* [1990], along with Doppler data from a network of stations. All these corrections were worked out as they are proposed in the GDR by *Cheney et al.* [1991].

Even though the new GDR was an improvement over the original one, additional processing was still necessary, mainly to "remove" the geoid, to minimize residual orbit error, to filter out unrealistic physical values, and to reduce the huge amount of data to gridded fields. This was done in the following five steps: (1) a "mean" sea level was obtained along each repeat track, ignoring small longitude departures (<1 km) of all repeats; (2) sea level anomalies (SLA) were subsequently computed; (3) along-track filtering was then performed; (4) along each track a first-order polynomial was fitted to the SLA and the linear trend was removed; and (5) SLA and derived surface geostrophic zonal current anomalies (ZCA) were finally gridded. These steps are detailed below, keeping in mind that all adjustable parameters (orbit correction scheme, time/space filter lengths, grid size, etc.) were chosen so that the ZCA approach in situ measurements of near-surface zonal current at three equatorial mooring locations (see section 4). This approach constitutes the most stringent test for validating Geosat in view of the sensitivity of the geostrophic approximation to small sea level perturbations near the equator.

In the first step the mean sea level was considered defined at any one position if at least 31 out of 43 possible values ranging within ±25,000 cm were present during the first 43 repeat cycles (November 8, 1986, to November 7, 1988); otherwise, no mean was computed. This 31/43 threshold is a compromise between having a minimum of values so that the mean is a meaningful quantity and having a sufficient spatial/temporal data coverage; it is similar to the 70% threshold used by *Zlotnicki* [1991] and *Fu et al.* [1991]. We note that the mean is computed over 2 entire years which include both an El Niño and a La Niña event so as to minimize a possible bias introduced by the seasonal and interannual variability. In the second step the mean was subtracted from each value, and only SLA ranging within ±150 cm were considered. In the third step, along-track slopes in SLA yielding surface geostrophic current anomalies faster than 2 m/s were excluded after being visualized. Then, following a technique described by *Picaut et al.* [1990], 200-km (total length) median and Hanning filters were applied to the along-track data, in order to suppress remaining nonphysical spikes [see *Picaut et al.*, 1990, Figure 2]. Also, data gaps smaller than 100 km were filled through linear interpolation. The fourth step consisted of removing a polynomial trend from the SLA along each 35°S–35°N track in order to minimize the residual orbit error. Sensitivity studies based on comparisons with in situ measurements (see section 4) led us to choose a first-order polynomial. This is consistent with the results of *Cheney et al.* [1989] which have shown that the orbit error can be modeled as a linear trend to a few centimeters over arcs as long as 10,000 km, given the radial precision of the new orbit (40 cm rms). In practice, long continuous arcs were sometimes not available owing to data gaps or near the periphery of the Pacific basin. Because computations of tilt and bias over short arcs could be ill defined or lead to elimination of oceanic signal, we plotted each arc shorter than 2500 km, compared it visually to its neighbors, and discarded obviously erroneous ones and ones that did not reach 1250-km length. Moreover, information about the arc length relative to each SLA was kept to be used further in the gridding procedure. At this stage of the processing we had "removed" the geoid and the 2-year average sea level (steps 1 and 2), the along-track wavelengths shorter than 200 km (step 3), and the orbit error (step 4).

The last step of our data processing was to summarize the huge amount of SLA data onto a regular space/time grid. Given our objectives and following *Delcroix et al.* [1991], we chose to grid the SLA data onto 0.5° latitude, 5° longitude, and 5-day bins covering the tropical Pacific from 28.5°S to 28.5°N, 125°E to 75°W (see Figure 1), and from November 23, 1986, to March 2, 1989. Note that reduction of the original space/time coverage results from filtering and quality control procedures; in particular, from March 1989 the amount of validated data collected by Geosat decreased dramatically owing to large solar activity [*Cheney et al.*, 1991]. To construct the three-dimensional grid, the SLA data were first grouped into 33, 10° overlapping longitude bands centered every 5° of longitude from 125°E to 75°W. In each longitude band the SLA were then grouped in 5-day bins and averaged every 0.5° latitude, each value being weighted both by its distance to the closest grid point and the length of the track from which it was issued. The SLA data were then gridded in time using a Laplacian interpolation scheme. Finally, the gridded SLA were smoothed with 3.5° latitude, 15° longitude, and 35-day Hanning filters to reduce small-scale noise resulting from time/space combination techniques.

2.2. Geosat-Derived Surface Geostrophic Current Anomaly

Given the SLA h, the anomalies of zonal surface geostrophic current u off and at the equator are expressed respectively as

$$fu = -gh_y \tag{1a}$$

$$\beta u = -gh_{yy} \tag{1b}$$

where f is the Coriolis parameter; β, its meridional derivative at the equator; g, the acceleration due to gravity; and the subscripts denote the first (y) and second (yy) derivatives in the meridional direction. Following *Picaut and Tournier* [1991], a correction factor $C(y)$ must be added to h to ensure continuity between u deduced from the first- and second-derivative calculations. The equatorially trapped correction factor $C(y)$ is expressed as:

$$C(y) = -(h_y)_{y=0}\, y e^{-y^2/L^2} \tag{2}$$

Given (1) and (2), the ZCA were calculated from the gridded SLA using first- and second-order, centered finite difference schemes off and right at the equator, respectively, with a trapping scale L of 2° latitude. It must be remembered that

Table 1. Comparison Between Geosat-Derived Sea Level and Zonal Current Anomalies Versus in Situ Measurements

Site	Location, Latitude, Longitude	N	R	rms_g	rms_i	G/I	rms_{dif}
		Sea Level Anomaly					
Kapingamarangi	1.1°N, 154.8°E	27	0.49	3.3	7.5	0.44	6.6
Pohnpei	7°N, 158.2°E	27.5	0.93	5.0	11.4	0.44	7.0
Mooring, mean TS	2°N, 165°E	14	0.58	4.3	5.9	0.72	4.9
with monthly TS		14	0.59	4.3	5.5	0.78	4.6
Mooring, mean TS	0°, 165°E	27	0.15	4.0	5.4	0.75	6.2
with monthly TS		27	0.47	4.0	4.6	0.87	4.5
Nauru	0.5°S, 166.9°E	27.5	0.65	4.2	7.1	0.60	5.4
Mooring, mean TS	2°S, 165°E	20.5	0.40	4.2	7.0	0.59	6.6
with monthly TS		20.5	0.64	4.2	5.9	0.71	4.6
Mooring, mean TS	5°S, 165°E	16	0.82	6.8	12.5	0.55	7.9
with monthly TS		16	0.88	6.8	11.0	0.62	6.0
Majuro	7.1°N, 171.4°E	26.5	0.86	5.8	8.8	0.66	4.8
Funafuti	8.5°S, 179.2°E	27.5	0.77	6.9	8.9	0.78	5.7
Kanton	2.8°S, 171.7°W	27.5	0.73	6.0	7.0	0.86	4.9
Penrhyn	9°S, 158°W	27.5	0.76	4.4	5.9	0.76	3.9
Christmas	2°N, 157.5°W	27.5	0.85	8.6	11.9	0.72	6.4
Mooring, mean TS	2°N, 140°W	15.5	0.86	6.4	10.7	0.55	6.2
Mooring, mean TS	0, 140°W	28	0.95	9.0	12.3	0.73	4.8
Mooring, mean TS	2°S, 140°W	21.5	0.93	7.2	8.8	0.82	3.4
Nukuhiva	8.9°S, 140°W	24	0.72	3.3	5.2	0.63	3.6
Mooring, mean TS	5°N, 110°W	24	0.77	6.2	8.4	0.74	5.4
Mooring, mean TS	2°N, 110°W	21.5	0.81	5.8	8.0	0.73	4.7
Mooring, mean TS	0°, 110°W	28	0.79	6.0	9.3	0.64	5.9
Mooring, mean TS	2°S, 110°W	22	0.70	5.7	8.7	0.66	6.2
Mooring, mean TS	5°S, 110°W	21	0.61	4.3	6.9	0.62	5.5
Santa Cruz	0.8°S, 90.3°W	27.5	0.46	3.3	8.2	0.40	7.3
Mean			0.74			0.67	5.3
		Zonal Current Anomaly					
Mooring, z = 50 m	0°, 165°E	24.5	0.92	41.9	41.9	1.0	16.6
Mooring, z = 10 m	0°, 140°W	27	0.70	30.7	31.7	1.0	24.0
Mooring, z = 10 m	0°, 110°W	28	0.49	29.3	32.3	0.9	31.4
Mean			0.70	34.0	35.3	1.0	24.0

Computed at each site is the length of the time series N in months, the correlation coefficient R, the rms of the Geosat-derived rms_g and in situ rms_i measurements, their ratio G/I, and the rms difference rms_{dif}. Dimensionalized units are centimeters and dynamic centimeters (mooring data) for sea level and centimeters per second for surface current.

the correction factor $C(y)$ does not alter the SLA and ZCA right at the equator ($y = 0$); it just smoothes out the ZCA within $\pm L$ degrees off the equator [see *Picaut and Tournier*, 1991, Figure 3].

3. Additional Data

Various supplementary data are used in the following discussion in order to assess the quality of Geosat-derived SLA and ZCA, as well as to help interpreting the ZCA during the 1986–1988 El Niño and La Niña period.

In situ comparisons of Geosat-derived SLA were performed from tide gauge measurements and 0/500-dbar dynamic height anomalies. Tide gauge sea level data were provided by the Tropical Ocean and Global Atmosphere (TOGA) sea level network [*Wyrtki et al.*, 1988]. Among all available sea level stations we selected 10 stations located within 10°N to 10°S, far from continental masses, and with almost continuous records from November 1986 to February 1989 (Figure 1 and Table 1). The sea level data consist of daily mean values that do not include the diurnal and semidiurnal tidal components. Instrumental uncertainties combined with island effects result in an error of 3–7 cm in the in situ sea level estimates.

In the open ocean, daily 0/500-dbar dynamic height anomalies were obtained from temperature sensors of 12 TOGA-Tropical Atmosphere Ocean (TAO) moorings located in the equatorial band at 165°E, 140°W, and 110°W (Figure 1 and Table 1). These "sea level" time series present the advantage of being evenly distributed in the equatorial wave guide, in contrast to sea level stations mainly located in the western half of the Pacific. The 0/500-dbar calculation was done, for all moorings, with *Levitus* [1982] mean TS relations and, for the moorings at 165°E, with monthly TS relations derived from 11 cruises [see *Delcroix et al.*, 1992]. Few short data gaps in the temperature time series at specific levels have been filled by extrapolation of neighboring levels using linear regression coefficients derived from overlapping time series; extrapolated values represent only 7% of the total values. It is interesting to note that the significance of our 0/500-dbar dynamic height anomaly is altered by the use of mean TS curve (at 110°W and 140°W) and 500-dbar reference level. The use of mean TS curves can result in a more than 5-cm error along 165°E [*Delcroix et al.*, 1987] and a 1-cm error at 110°W [*McPhaden and Hayes*, 1990]. Density variations below 500 dbar would result in about a 1- to 2-cm error when using 500 dbar as an absolute reference level. Compared with this, errors introduced by discrete vertical temperature sampling along the mooring lines appear negligible. Following the Geosat data processing, all daily sea level and

0/500-dbar dynamic height anomaly data were averaged over 5-day bins and low-pass filtered with a 35-day Hanning filter, and anomalies were computed relative to the 2-year period November 1986 to October 1988.

In situ comparisons of Geosat-derived ZCA were also performed from currents measured from three taut-line surface moorings located along the Pacific equator at 165°E, 140°W, and 110°W. Each surface mooring was instrumented in the upper 250–300 m with six to seven vector averaging current meters (VACM). The VACM recorded 5-min average currents which were processed to daily average in a manner similar to that described by *Freitag et al.* [1987]. The shallowest records with a minimum of 1-year duration were used for each mooring for comparison with Geosat-derived ZCA. The current data at 50-m depth were selected for 0°–165°E and at 10-m depth for 0°–140°W and 0°–110°W. As already noticed by *McPhaden et al.* [1990], we found the 50-m current variability at 165°E representative of the flow at 10 m; the correlation coefficient between daily averaged 10- and 50-m data is 0.83 for 893 common measurements in 1986–1991, with a rms difference of 18 cm/s. A 7-month data gap at 140°W was filled in by extrapolating 25-m data to 10 m, based on linear regression fit of 10- and 25-m daily values; the correlation coefficient between 10- and 25-m data is 0.96 for 1916 common measurements in 1984–1991, with a rms difference of 11 cm/s. To conform with the Geosat data processing, current time series were processed into 5-day bins and filtered in time with a 35-day Hanning filter, and anomalies were computed relative to the 2-year period November 1986 to October 1988.

To help understand the ZCA changes, we also used the Florida State University (FSU) wind field analysis [*Goldenberg and O'Brien*, 1981]. The original monthly 2° latitude by 2° longitude wind field was smoothed with a 14° longitude Hanning filter to approach the Geosat data processing. We also commented on two indicators of ENSO obtained from the Climate Analysis Center (Washington, D. C.), the Southern Oscillation Index (SOI) (as defined in Plate 2) and the SST averaged in the Niño3 region (5°S–5°N, 150°W–90°W). Monthly anomalies of SST in the Niño3 region (hereinafter defined as SSTA) were calculated relative to the 2-year period November 1986 to October 1988.

4. In Situ Comparisons

Comparisons between Geosat-derived and in situ sea level and surface currents were performed to assess how well Geosat data capture the variability of these two quantities.

4.1. Geosat-Derived and in Situ Sea Level

Statistical comparisons between Geosat-derived and in situ sea level measurements are given in Table 1, and sea level time series at the equator and 110°W, 140°W, and 165°E are exemplified in Figure 2. From Table 1 we see that the Geosat SLA are in reasonably good agreement with in situ measurements, with averaged correlation of 0.74, rms difference of 5.3 cm, and signal ratio (defined as the rms Geosat signal over the rms in situ signal) of 67%. These values are the same order of magnitude as the ones found by *Chao et al.* [1993] for somewhat different locations. It is worth noting that the best correlations, the smallest rms differences, and the signal ratios closest to 1 are obtained in the central basin, suggesting that interpretation of our Geosat data for the far eastern and western equatorial Pacific must be viewed with some caution. Also, it is worth noting that the Geosat signals appear damped at all locations (67%, on average), as exemplified in Figure 2 along the equator. This may reflect that Geosat sea level data are averaged over 10° longitude by 0.5° latitude and smoothed with a 3.5° latitude and 15° longitude Hanning filter, in contrast to in situ data. Note that a sensitivity study was performed by using either bias only or quadratic orbit error correction schemes, and this did not improve, but rather degraded, the mean signal ratio. A thorough investigation of the specific processes contributing to the differences between Geosat and in situ measurements is beyond the scope of this paper.

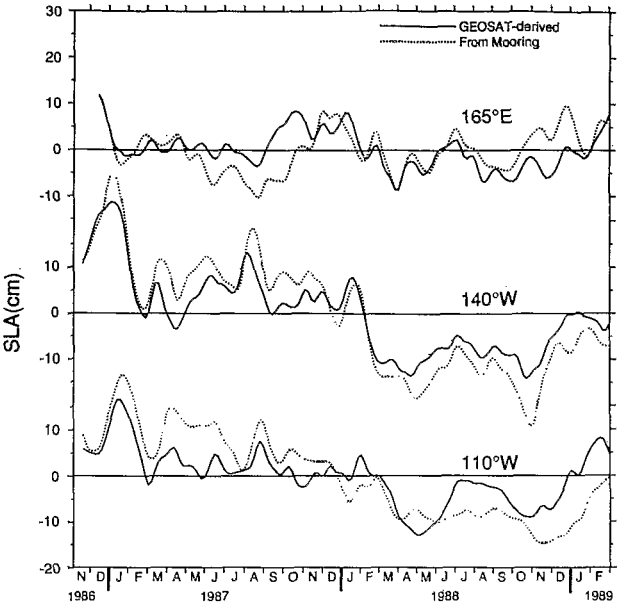

Figure 2. Comparisons between Geosat-derived sea level anomalies and 0/500-dbar dynamic height anomalies at the equator and (top) 165°E, (middle) 140°W, and (bottom) 110°W. Units are in centimeters.

4.2. Geosat-Derived and in Situ Surface Current

Time series of Geosat-derived and in situ ZCA are shown in Figure 3 for each equatorial mooring, along with basic statistical coefficients which are provided in Table 1. In agreement with *Picaut et al.* [1990], but with the addition of 15 months of measurements, the calculated and observed currents present a good correspondence at 165°E and 140°W. The correlation coefficients between the two time series are 0.92 (165°E) and 0.70 (140°W), with corresponding rms differences of 17 and 24 cm/s, compared respectively with the 42 and 32 cm/s rms of the observed currents. Also, the ratios of the rms calculated currents over the rms observed currents are close to 1 for each mooring. These comparisons indicate that low-frequency variations of zonal surface currents at 0°–165°E and 0°–140°W can be fairly well deduced from Geosat data during the ERM. It is worth noting that the Geosat-derived ZCA seem slightly overestimated during the El Niño period (November 86 to November 87), when the zonal wind stress anomalies are eastward, and slightly underestimated during the La Niña period (after November 87), when the zonal wind stress anomalies are westward. This may reflect the effect of wind-induced frictional velocity

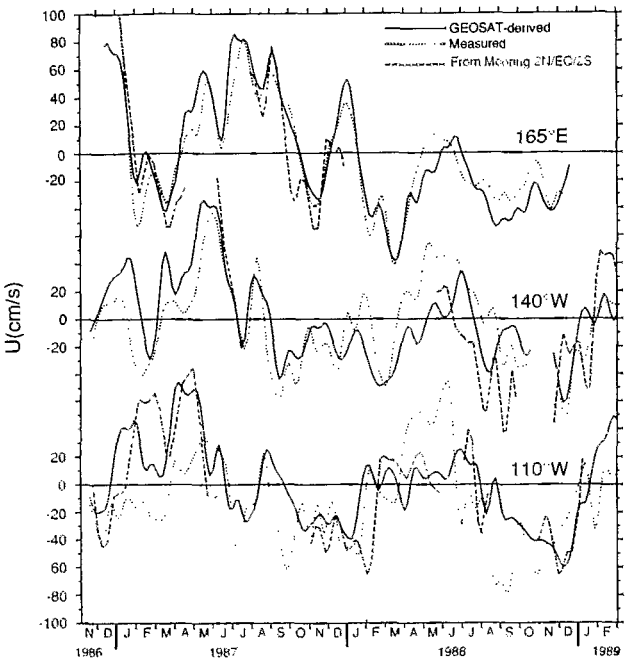

Figure 3. Comparisons between zonal Geosat-derived surface current anomalies (solid line), near-surface measured current anomalies (dotted line), and surface current anomalies deduced from the 0/500-dbar dynamic height curvatures (P_{yy}) obtained from the 2°N, 0°, 2°S mooring data (dashed line). The comparisons are presented at the equator and (top) 165°E, (middle) 140°W, and (bottom) 110°W. The mean near-surface measured currents over the November 1986 to October 1988 reference period are −2, −14, and −17 cm/s for 165°E, 140°W, and 110°W, respectively. Positive current anomalies are eastward. Units are centimeters per second.

which contributes to the measured ZCA but not to the Geosat-derived ZCA deduced from geostrophy.

A similar comparison performed at 110°W is less convincing (Figure 3). Although the ratio of the rms calculated currents (29 cm/s) over rms observed currents (32 cm/s) is close to 1, the correlation coefficient is only 0.49 and the rms difference (31 cm/s) is of the same order of magnitude as the rms observed current. As noticed by *Picaut et al.* [1990], part of the discrepancy could be explained by the fact that descending tracks near 0°–110°W are sometimes not present at the time of the observations, therefore reducing the optimum temporal resolution (80%, on average) and the efficiency of the low-pass filter. However, Figure 3 reveals that large discrepancies between the time series occur during March–June 1987 and 1988, at a time of large eastward surface current associated with the surfacing of the Equatorial Undercurrent. Interestingly, the March–June discrepancies do not exist when comparing Geosat-derived ZCA with another geostrophic in situ ZCA derived from 0/500-dbar dynamic height curvature P_{yy} obtained from the 2°N, 0°, and 2°S mooring data. In this latter comparison the correlation coefficient is 0.78 (0.88 at 0°–165°E, 0.79 at 0°–140°W) with a rms difference of 24 cm/s (21 cm/s at 0°–165°E, 34 cm/s at 0°–140°W). Since Geosat-derived and 2°N/0°/2°S mooring-derived ZCA are both derived from geostrophic relations, in contrast to the directly measured ZCA, this suggests that the poor agreement at 0°–110°W may not only be linked to the poor density of the surrounding Geosat data, but may also reflect dynamic reasons. The reason for this is unclear and deserves further investigation.

5. Geosat-Derived Variabilities

5.1. The Sea Level

The spatial distribution of the rms of SLA about the 2-year period from November 1986 to October 1988 is given in Figure 4. The rms is greater than 4 cm over most of the tropical Pacific, except north of 15°N, in the far eastern and western equatorial Pacific and in the southeastern Pacific. The largest rms appears in the central Pacific, 110°–180°W, with one maximum trapped at the equator and a second one along a zonal band near 10°–12°N. Moreover, the rms presents two maxima west of the date line, on both sides of the equator at 4–12° latitudes. As reported by *White and Tai* [1992] and *Chao et al.* [1993], this rms distribution mostly results, in the central Pacific, from the combined effects of the seasonal and interannual variability and, west of the date line, from the interannual variability associated with the 1986–1989 El Niño and La Niña events. We also note that the present rms distribution is similar to the one obtained using 1970–1987 time series of the depth of the 20°C isotherm, a proxy for sea level [*Kessler*, 1990].

The longitude–time plot of SLA along the equator (Plate 1b) reveals eastward propagation of SLA with mainly positive SLA during the El Niño period, November 1986 to February 1988, and negative SLA during the La Niña period, from March 1988. Along 4°S and 4°N latitudes (Plates 1a and 1c) the SLA propagate westward with roughly semiannual alternation of positive and negative SLA, more easily discernible along 4°N. Similar results have been obtained by *Delcroix et al.* [1991] and *Fu et al.* [1991, 1993]. Along the equator, time lag correlation matrix analysis yields a mean eastward phase speed $c_K = 3.1 \pm 0.5$ m/s (the second number is 1 standard deviation), indicative of a first baroclinic Kelvin mode. Along 4°N/4°S the mean westward phase speed is $c_R = 1.0 \pm 0.3$ m/s; it corresponds to the theoretical phase speed $c_K/2m + 1$ of the first symmetric ($m = 1$) Rossby wave. Interestingly, we confirm the dominance of the first baroclinic mode.

5.2. The Surface Current

The spatial distribution of the rms of ZCA is given in Figure 4b. The rms is greater than 10 cm/s inside a zonal band ranging from about 8°N to 8°S, reduced to 4°N to 4°S near the eastern Pacific coast. As expected from geostrophy, the rms values increase equatorward, to reach as much as 40 cm/s at or close to the equator. The maximum values appear trapped at the equator, in the western half of the basin, where surface current reversal is frequently observed [*Delcroix et al.*, 1992], and in the eastern half of the basin, slightly displaced to the north near the shear zone between the South Equatorial Current and North Equatorial Countercurrent. The magnitude of these Geosat-derived rms is in excellent agreement with observational results based on mooring data (see Table 1), drifting buoys [*Hansen and Paul*, 1984, Figure 5], and XBT data [*Tournier*, 1989, Figure 24].

The near-equatorial rms maxima displayed in Figure 4b occur at latitudes corresponding to the location of peak amplitude in equatorial Kelvin and $m = 1$ Rossby modes, suggesting, in agreement with the SLA in Plate 1, that these

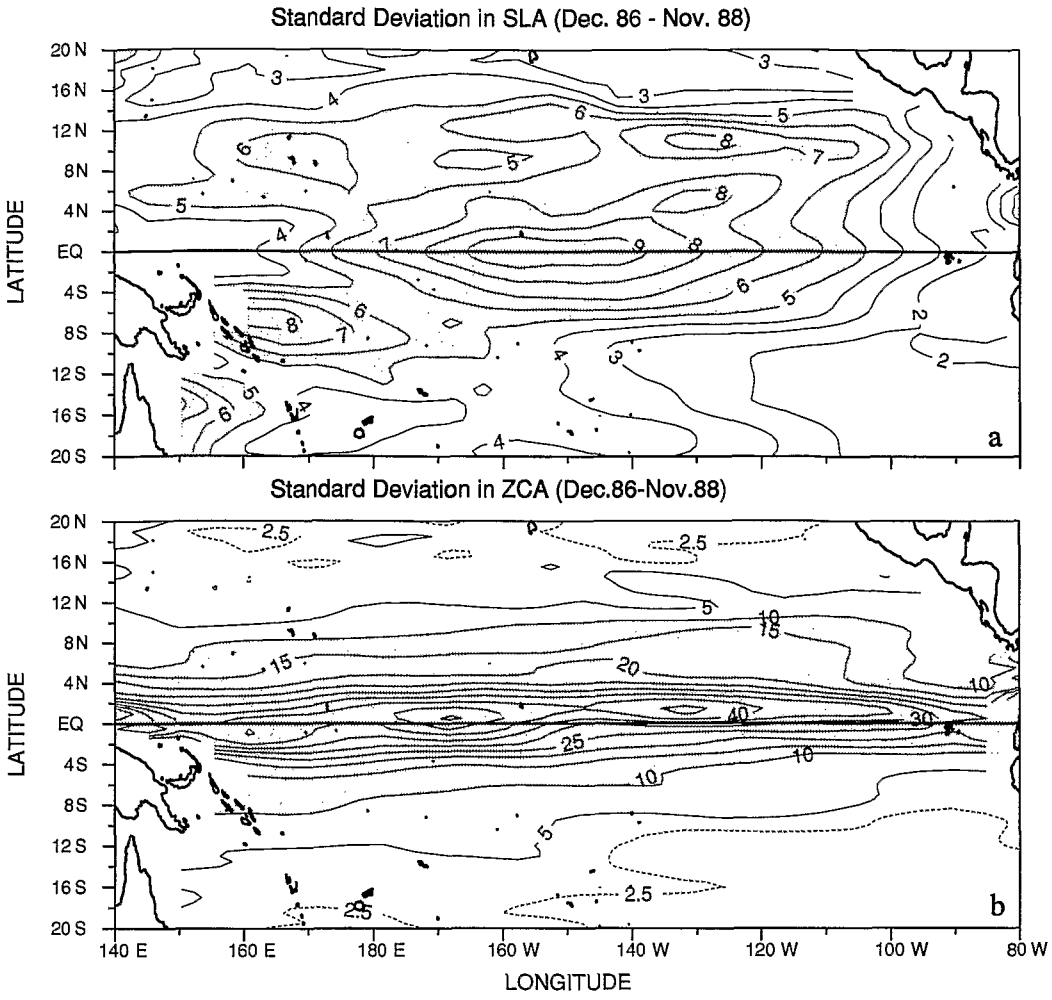

Figure 4. Maps of the standard deviation of (a) sea level anomalies (in centimeters) and (b) surface zonal current anomalies (in centimeters per second). Shaded areas denote values greater than (top) 5 cm and (bottom) 10 cm/s. The contour intervals are (top) 1 cm and (bottom) 5 cm/s, except for the 2.5-cm/s dotted lines.

modes may play an important role in the evolution of ZCA. (It needs to be kept in mind that U on Figure A1 is maximum at the equator in terms of Kelvin and $m = 1$ Rossby modes). As a consequence, we now put the emphasis on the signature of Kelvin and Rossby waves, in terms of ZCA.

6. Synopsis of Kelvin and Rossby Modes in Zonal Current and Wind Forcing

6.1. The Kelvin and Rossby Modes in Zonal Current Anomaly

To identify the signature of first baroclinic Kelvin and Rossby waves as the ones identified in Plate 1, the ZCA is projected into equatorial orthogonal modes (see appendix), restricting our attention to the Kelvin, first symmetric ($m = 1$), first antisymmetric ($m = 2$), and second symmetric ($m = 3$) meridional Rossby modes. Figure 5 shows the 160°E–90°W zonally averaged rms of the ZCA and the cumulative contributions of the Kelvin, $m = 1$, $m = 2$, and $m = 3$ Rossby modes. The zonally averaged rms of the ZCA ranges within 10 to 20 cm/s near 4° latitudes, where it decreases almost linearly poleward. Within 4°N–4°S it is roughly a bell-shaped function with the peak at 1°N. Most importantly, the cumulative contribution of the Kelvin and $m = 1$ Rossby modes is almost identical to the total rms, meaning that these two modes contribute equally to most of the rms in ZCA. A statistical study reveals that within 4°N–4°S (a bit more than one radius of deformation of the first baroclinic mode off the equator), 71% of the total variance in ZCA can be accounted for by the contribution of the Kelvin and $m = 1$ Rossby modes. This percentage increases to 85% when we also consider the $m = 2$ Rossby mode, which is responsible for the slight northward shift of the total rms of ZCA in Figure 5.

Clearly, Figures 4 and 5 indicate that the zonal current within 4°N–4°S is the most energetic anywhere and that its variability can be fairly well reproduced using only the Kelvin and $m = 1$ Rossby modes. Moreover, modeling studies involving the delayed action oscillator mechanism

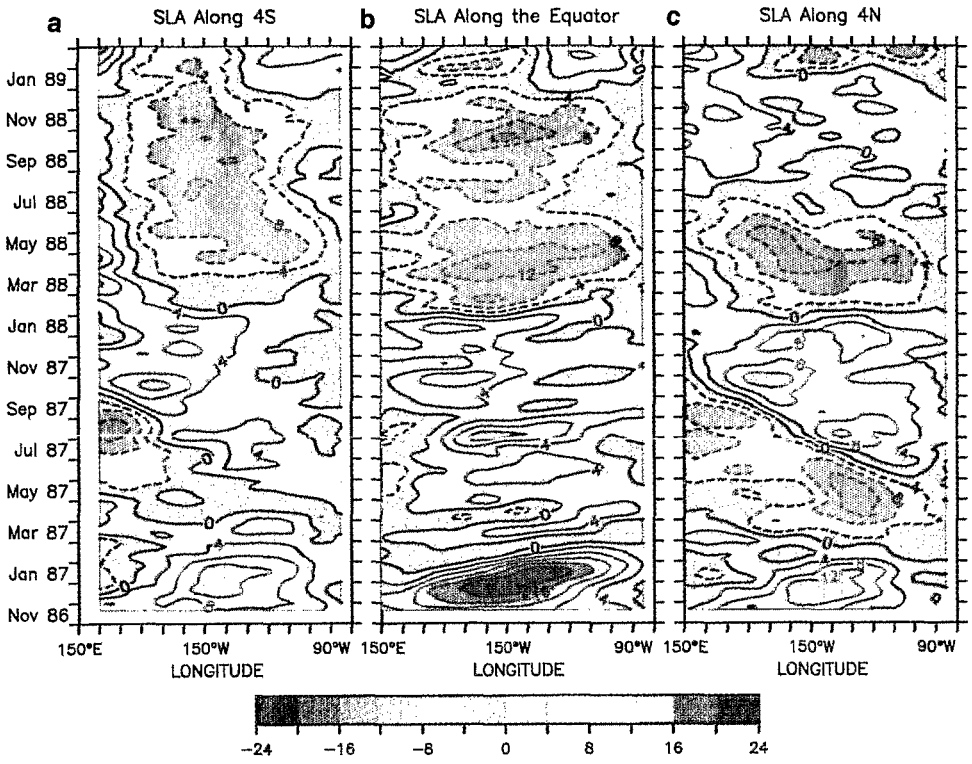

Plate 1. Longitude–time plots of sea level anomalies (SLA) along (a) the 4°S latitude, (b) the equator, and (c) the 4°N latitude. Contour intervals are 4 cm.

[*Battisti*, 1988; *Wakata and Sarachik*, 1991] suggest that these two modes are very important in the ENSO cycle. As a consequence, we now focus on these two modes only.

6.2. The Kelvin and Rossby Modes in the Wind Forcing

The projection of normalized zonal wind anomaly onto the Kelvin mode, as detailed in the appendix, is shown in Plate 2a. The projection of the zonal wind anomaly onto the m = 1 Rossby mode is not shown here. As discussed by *Wakata and Sarachik* [1991], it has almost the same pattern as in Plate 2a but of opposite sign and about half ($\sim 2^{1/2}/3$) the amplitude. As a consequence, it is useful to note that a westerly Kelvin wave forcing, i.e., a positive value on Plate 2a tends to build up downwelling Kelvin and upwelling Rossby waves with both eastward ZCA signature, i.e., a positive value on Plates 3b and 3c and vice versa. Because it is almost identical to the zonal wind anomaly observed in the equatorial band, the Kelvin wave forcing will be hereafter defined as the zonal wind anomaly. Schematically, we observe westerly (easterly) wind anomaly west (east) of 130°W during El Niño and, conversely, easterly (westerly) wind anomaly east (west) of 130°W during La Niña. A more thorough description is given in the following section.

7. Chronology of the Zonal Current Anomaly Near the Equator

The longitude–time plot of the ZCA along the equator (Plate 3a) shows that El Niño is mostly characterized by the dominance of eastward ZCA, whereas La Niña is mostly characterized by the dominance of westward ZCA. During the whole period, in agreement with Plate 1, we note the occurrence of both eastward and westward propagation of ZCA, reflecting the competing influence of Kelvin and m = 1 Rossby modes. The longitude–time plots of these two modes along the equator is given in Plates 3b and 3c, keeping in mind that off-equatorial contribution can be deduced from Figure A1. Plate 3b shows that downwelling Kelvin waves appear mainly during El Niño, whereas upwelling Kelvin waves appear mainly during La Niña. In agreement with the SLA, Plate 3c shows the semiannual alternation of upwelling and downwelling m = 1 Rossby waves during the whole period, consistent with the normal seasonal cycle [*duPenhoat et al.*, 1992], but with enhanced amplitude. Interest-

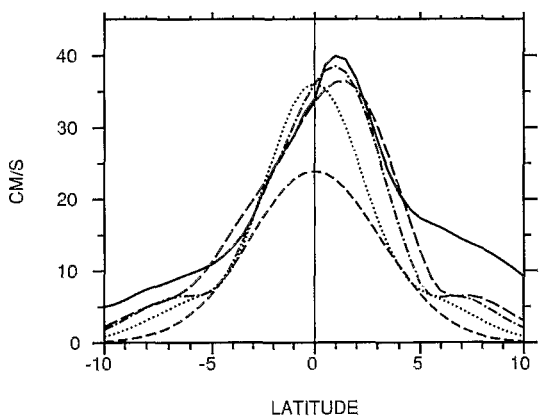

Figure 5. Meridional distribution of the 160°E–90°W averaged standard deviation for the surface zonal current anomaly (ZCA) (solid line) and the cumulative contributions of the Kelvin (short-dashed line), first symmetric Rossby (dotted line), first antisymmetric Rossby (dash-dotted line), and second symmetric Rossby modes (long-dashed line).

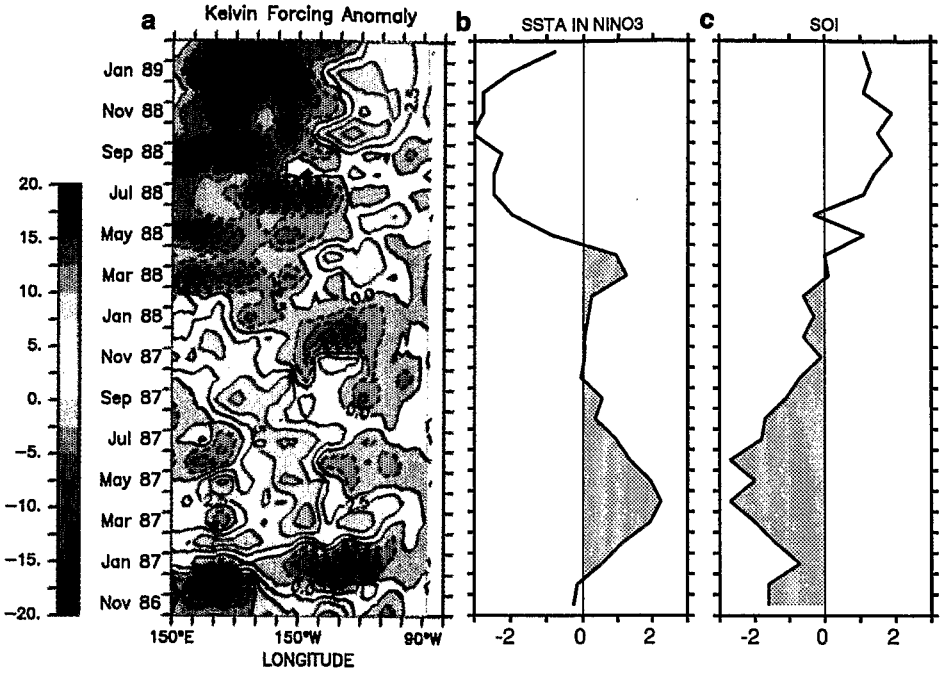

Plate 2. (a) Longitude–time plot of the projection of the zonal wind anomalies onto the Kelvin mode. Units are nondimensionalized (see the appendix); note that 2.5 units roughly correspond to 10 m^2/s^2 zonal pseudostress at the equator. Contour intervals are 2.5 units. Positive values denote westerly Kelvin forcing anomaly. (b) Monthly sea surface temperature anomalies (SSTA) relative to the 2-year period November 1986 to October 1988, averaged in the so-called Niño3 region (5°S–5°N, 150°W–90°W). Units are degrees Celsius, and positive values are shaded. (c) Monthly Southern Oscillation Index (SOI) defined as the differences between the standardized sea level pressure anomalies at Tahiti and Darwin (Tahiti minus Darwin). Values are normalized by the mean annual standard deviation. Negative values are shaded.

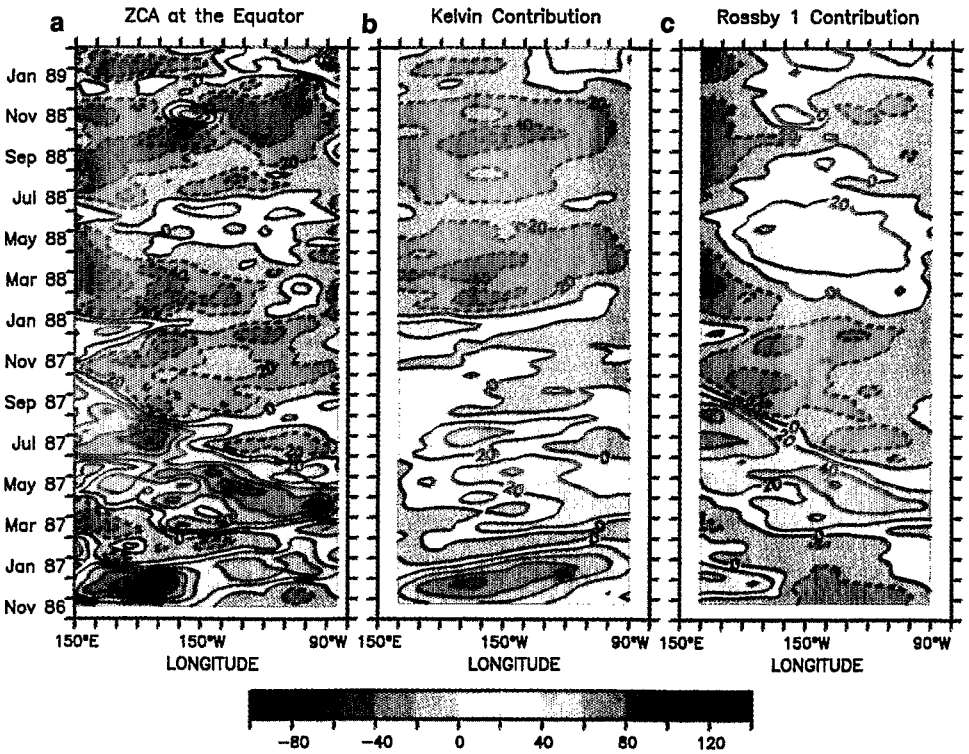

Plate 3. Longitude–time plots along the equator of (a) the surface zonal current anomalies (ZCA), (b) the ZCA projected onto the first baroclinic Kelvin mode, and (c) the ZCA projected onto the first symmetric Rossby mode. Contour intervals are 20 cm/s.

ingly, time lag correlation matrix analysis performed between 180° and 100°W on Plates 3b and 3c yields phase speeds of 3.1 ± 0.8 and 1.1 ± 0.3 m/s, respectively. Once again, this justifies a posteriori using the first baroclinic mode phase speed (c = 2.8 m/s) to project the ZCA.

With this overall view in mind we now turn to a detailed description of the ZCA near the equator during 1986–1988, to be identified in terms of Kelvin and first symmetric Rossby modes.

7.1. The El Niño Period

At the beginning of the analyzed time series, November 1986, the SSTA (still defined in the Niño3 region) was close to zero, although the SOI was already negative (Plates 2b and 2c), reflecting that the large-scale trade wind has started to decrease for 3–4 months [*Delcroix et al.*, 1992, Figure 9], following *Wyrtki*'s [1975] ENSO scenario.

In December 1986 a large and strong patch of westerly wind anomaly occurred in the warm pool region, west of 170°W, with the highest value centered near the date line (Plate 2a). Concomitant with this patch was the appearance of a well-marked downwelling Kelvin wave; it propagated all the way to the eastern boundary and had a ZCA signature of the order of 40–80 cm/s (Plate 3b). *Delcroix et al.* [1991] have also highlighted this strong downwelling Kelvin wave in SLA through time lag correlation analysis (c = 2.8 m/s) and least squares fits of its meridional structures at different longitudes (c = 2.3 m/s). Still in December 1986, consistent with the zonal wind anomaly, was a hint in Plate 3c of an upwelling Rossby wave propagating westward from 170°W.

In January 1987 the strong downwelling Kelvin wave reached the eastern Pacific coast when it encountered unfavorable easterly wind anomaly (Plate 2a). Model results suggest that this wind anomaly prevents the downwelling Kelvin wave from reflecting [*duPenhoat et al.*, 1992], yet no sign of reflection was seen in our observations. The January 1987 easterly wind anomaly not only existed in the eastern basin, but also as far as the warm pool region where Plate 3b reveals its possible effect in triggering a weak upwelling Kelvin wave of 10 cm/s westward ZCA.

In early March 1987 the weak upwelling Kelvin wave passed the Galapagos Islands. At that time, westerly wind anomaly had resumed in the western Pacific. As expected from theory, our observations suggest that this westerly wind anomaly induced a March 1987 downwelling Kelvin wave starting from about 160°W and of 20 cm/s eastward ZCA. Most importantly, the westerly wind anomaly strengthened toward the eastern boundary, probably in relation to the SSTA increase (Plate 2b) associated with the reduction of the seasonal upwelling [e.g., *Delcroix*, 1993] and/or the thermocline depression resulting from the strong downwelling and weak upwelling Kelvin waves acting in opposition, with the former dominating. As a possible result of this westerly wind anomaly, a March–September 1987 strong upwelling Rossby wave propagated across the whole equatorial basin with 40–80 cm/s eastward ZCA (Plate 3c). Given the large amplitude of this Rossby wave, it was even evident in the earlier, less accurate Geosat data [*Delcroix et al.*, 1991]. Interestingly, *duPenhoat et al.* [1992] demonstrated that in their model the reflection of the weak upwelling Kelvin wave weakly contributes to this strong upwelling Rossby wave and makes it visible all the way from the eastern to the western Pacific. At the eastern boundary the timing of our observed upwelling Kelvin and Rossby waves agrees with their results.

From April to November 1987 the westerly wind anomaly prevailed in the central Pacific as long as SSTA remained positive (Plate 2b). During that period a series of downwelling Kelvin waves was being produced with eastward ZCA of 20–50 cm/s (Plate 3b). Namely, three main downwelling Kelvin waves propagated from 170°–180°W, respectively, in May/June (20–40 cm/s ZCA), July/August (20–60 cm/s ZCA), and the last one in October/November 1987 with the lowest ZCA. These three downwelling Kelvin waves obviously arose in SLA (Plate 1b), and the second one was noted by *Delcroix et al.* [1991]. Surprisingly, given the 1-month resolution of the original wind field, the patches of maximum westerly wind anomaly, 5 to 7.5 units in Plate 2a, closely coincide with the three observed downwelling Kelvin waves. We note that the July/August downwelling Kelvin wave emanates from about 170°W where and when the FSU wind field analysis shows easterly wind anomaly. Direct wind measurements, however, conflict with this FSU analysis. Strong westerly winds were observed at 0°–165°E in June and July [*McPhaden et al.*, 1990] and from 4°S–3°N during the Surtropac 8 cruise along 165°E from July 9 to 12 [*Delcroix et al.*, 1992].

7.2. The Transition Period

The October/November 1987 downwelling Kelvin wave, the last of the El Niño downwelling Kelvin wave series, entered the central Pacific when the SOI and the SSTA returned to zero (Plates 2b and 2c). Then, this downwelling Kelvin wave encountered easterly wind anomaly, which apparently severely reduced its amplitude and prevented it from reaching the eastern Pacific. To a certain extent, the easterly wind anomaly seems to reinforce a downwelling Rossby wave which could have left the eastern Pacific in June/July 1987, as easterly wind anomaly built in phase with the normal seasonal cycle.

From November 1987 to February 1988 the central Pacific westerly wind anomaly decreased while the SSTA was close to zero. This gave way to easterly wind anomaly which seems instrumental in forcing another downwelling Rossby wave. This wave encountered continuous, favorable easterly wind anomaly while propagating to the western boundary, which it reached in March/April 1988. Besides, as the zonal wind anomaly increased westward in the western Pacific, during November/December 1987, a downwelling Kelvin wave was produced, closely in phase with the normal seasonal cycle [*duPenhoat et al.*, 1992]. Its eastward ZCA signature, 10–30 cm/s, counteracted in the west and reduced in the east the westward ZCA associated with the previously mentioned downwelling Rossby wave.

7.3. The La Niña Period

The SOI crossed zero from negative to positive values in March 1988 (Plate 2c). In contrast, the SSTA became positive again, in phase with the normal seasonal cycle [e.g., *Delcroix*, 1993], and perhaps as a result of the early 1988 seasonal downwelling Kelvin wave which may have acted to warm the SST in moving the cold water away from the surface (although its effects should be weak because the upwelling is minimum at this time). The return of positive SSTA in March 1988 corresponded to the occurrence of westerly wind anomaly in the eastern half of the basin.

Following this, the SSTA became frankly negative and the westerly wind anomaly in the eastern Pacific migrated eastward to July 1988 when its amplitude fell to zero. As long as this westerly wind anomaly existed, during March–July 1988, upwelling Rossby waves continued to be produced from the eastern Pacific, with westward ZCA signature of the order of 10–30 cm/s.

In contrast to March–April 1987, when westerly wind anomaly occupied almost the whole basin, the positive SSTA in March–April 1988 coincided with westerly wind anomaly in the east but not in the west. In fact, easterly wind anomaly prevailed in the western half of the Pacific, probably in relation to the westward return of the warm pool under the 6-month cumulative effects of westward ZCA associated mainly with the previously noted downwelling Rossby wave. *McPhaden and Picaut* [1990] with direct velocity measurements at 0°–165°E and J. Picaut and T. Delcroix (Equatorial wave sequence associated with the warm pool displacement during the 1986–1989 El Niño and La Niña, submitted to *Journal of Geophysical Research*, 1994) (hereinafter referred to as Picaut and Delcroix, submitted manuscript, 1994) with the present basin-wide ZCA bolster this explanation.

Between March 1988 and the end of 1988 the SSTA reached its coldest values since 1975 and the easterly wind anomaly correspondingly persisted in the west, up to the end of the analyzed time series. With the persistence of easterly wind anomaly a series of upwelling Kelvin waves was generated from the warm pool region. Two main upwelling Kelvin waves are clearly discernible in ZCA, as well as in SLA (Plate 1b), with eastward ZCA signature of 20–50 cm/s (Plate 3b). The first main upwelling Kelvin wave started near the date line in March 1988, concurrent with a strong patch of easterly wind anomaly (>7.5 units on Plate 2a). It encountered favorable easterly wind anomaly while propagating to the central basin, and it reached the eastern basin in May 1988 as the SSTA cooled rapidly. The second main upwelling Kelvin wave arose near the date line, in September 1988, almost simultaneously with the strongest recorded easterly wind anomaly (>10 units on Plate 2a). As did the first main upwelling Kelvin wave, this second upwelling Kelvin wave propagated all the way to the east, most of the time accompanied by favorable wind forcing, and it likely contributed to increasing the cooling of the SSTA at the time of strong upwelling. Plate 2a shows other strong patches of easterly wind anomaly (>7.5 units), in particular the one centered at 150°W in July 1988; this corresponds to a relative maximum in eastward ZCA, but its eastward propagation is not clear.

At the end of the analyzed time series, in early 1989, easterly and westerly wind anomaly still prevailed in the western and eastern halves of the equatorial Pacific, respectively. Then, consistent with the wind forcing, Plates 8b and 8c show, in the western half of the basin, an upwelling Kelvin wave with eastward ZCA of 10–20 cm/s, and, in the eastern half, a downwelling Rossby wave with westward ZCA of 10–20 cm/s, both resulting in a mean ZCA close to zero at the 0°–140°W mooring location (Figure 3). By January 1989 the SOI was still positive and then decreased to zero, which was only reached by the end of 1989 (not shown here). The SSTA, however, began to rise sharply in early 1989, in phase with the normal seasonal cycle, heralding the progressive demise of the cold event.

8. Summary and Discussion

A comprehensive description of low-frequency sea level anomalies (SLA) and surface geostrophic zonal current anomalies (ZCA) in the tropical Pacific was made possible with altimeter data pertaining to the first 2 1/2 years of the Geosat 17-day Exact Repeat Mission (November 8, 1986, to March 2, 1989). To this end, the recently improved Geosat geophysical data records [*Cheney et al.*, 1991] were processed carefully through various steps, with the idea to best fit the derived ZCA to in situ, near-surface zonal current observations at three equatorial mooring locations (165°E, 140°W, and 110°W).

Once confidence was gained in Geosat-derived ZCA (and SLA), the emphasis was put on the equatorial wave guide where ZCA are more energetic than anywhere. Projecting the observed ZCA onto equatorial first baroclinic meridional modes, it was first demonstrated that the cumulative contribution of Kelvin and first symmetric ($m = 1$) Rossby modes matches the observed 4°N–4°S variability fairly well. Owing to the importance of these two modes in ENSO cycle models, the chronology of the ZCA in the equatorial wave guide was then interpreted in terms of Kelvin and $m = 1$ Rossby modes during the 1986–1987 El Niño and the ensuing 1988–1989 La Niña.

The 1986–1989 complete ENSO cycle was divided into three periods, relying on ENSO indicators such as the Southern Oscillation Index (SOI), the SSTA in the Niño3 region (5°N–5°S, 150°W–90°W), and the occurrence of basin-wide mean eastward and westward ZCA. The first period, the 1986–1987 El Niño, is characterized by a strong downwelling Kelvin wave in December 1986 to January 1987, a series of downwelling Kelvin waves in March–October 1987, and a strong $m = 1$ upwelling Rossby wave in March–September 1987. Of main interest, these waves are all consistent with the zonal wind anomaly forcing. Moreover, they all gave rise to notable eastward ZCA for almost an entire year during the 1986–1987 El Niño, as was modeled during the 1972–1973 [*Gill*, 1983] and 1982–1983 [*Bigg and Blundell*, 1989] El Niño events. The second period, the transition, reveals the occurrence of two $m = 1$ downwelling Rossby waves originating from the eastern Pacific at times of favorable zonal wind anomaly forcing. These downwelling Rossby waves, propagating in the second half of 1987 and early 1988, acted to switch the basin-wide mean ZCA from eastward to westward. This terminated the warm event, El Niño, and gave rise to the subsequent cold event, La Niña. The third period, La Niña, shows the generation of a series of upwelling Kelvin waves, clearly identified in March/April and September/October 1988. These upwelling Kelvin waves are apparently in close relation with the advent and persistence of easterly wind anomaly in the western half of the basin, from March 1988 to early 1989. The occurrence of this easterly wind anomaly in the west seems associated with the anomalous westward displacement of the warm pool produced by the westward ZCA during the transition period. In contrast with the El Niño period, these upwelling Kelvin waves yielded to the dominance of basin-wide mean westward ZCA for more than 1 year, this ZCA being slightly reduced by a front of $m = 1$ upwelling Rossby waves in phase with the normal seasonal cycle.

Interestingly, the zonal wind anomaly forcing appears repeatedly as the main source for Kelvin and $m = 1$ Rossby

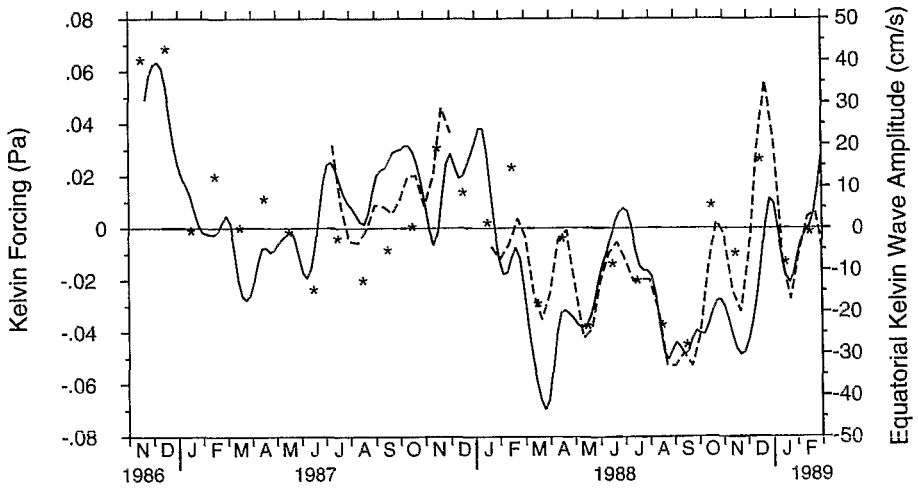

Figure 6. Time series of 130°E–160°E averaged Kelvin forcing anomaly derived from the special sensor microwave imager (dashed line) and Florida State University wind products (stars) and equatorial Kelvin amplitude at 0°–160°E (solid line).

waves which both mostly govern the ZCA within 4°N–4°S. In the eastern half of the basin we noted that the zonal wind anomaly is closely related to the enhanced/reduced SST seasonal cycle during El Niño/La Niña, respectively. In the western half of the basin we suspected a tight relation between the zonal wind anomaly and the zonal displacement of the eastern edge of the warm pool resulting from the ZCA signature of Kelvin and Rossby waves forced by the zonal wind anomaly itself. Clearly, the way sea surface temperature, surface zonal current associated with Kelvin and m = 1 Rossby waves, zonal wind anomaly, and zonal displacement of the warm pool in the equatorial band combined to constructively build the 1986–1989 El Niño and La Niña cycle deserves further in-depth investigations, to be dealt with in another paper (Picaut and Delcroix, submitted manuscript, 1994).

At this point, comparing our analysis with modeling results is instructive. Most importantly, we would like to emphasize the repeated time/space coincidence of observed favorable wind forcing with observed Kelvin and m = 1 Rossby waves. In other words, our analysis of a peculiar ENSO cycle was made without the need to take into account eastern and/or western boundary reflections. Still, at the eastern boundary, Plates 3b and 3c indicate possibilities for the upwelling Kelvin waves arriving around March 1987 and May 1988 (ZCA < 0) to reflect into upwelling Rossby waves (ZCA > 0). There is also a hint in Plates 3b and 3c that the downwelling Kelvin waves (ZCA > 0) arriving in June 1987 might reflect as downwelling Rossby waves (ZCA < 0). Modeling results indeed suggest these eastern boundary reflections, at least during El Niño, although they would only contribute weakly in sending Rossby waves back to the central Pacific [*duPenhoat et al.*, 1992].

As noted in section 4.1, the relatively poor quality of the Geosat data near the western Pacific rim prevents us from exploring the evolution of Rossby waves west of 160°E longitude. However, at this longitude the sign of the ZCA in Plates 3b and 3c shows that a possible western boundary reflection could occur in December 1987 when a downwelling Rossby wave (ZCA < 0) might reflect as a downwelling Kelvin wave (ZCA > 0). If factual, then this western boundary reflection would yield eastward ZCA that would tend to plunge the ocean into a warm event, contrasting with the delayed oscillator theory, where reflections of upwelling Rossby wave into upwelling Kelvin wave act to terminate the warm event.

In order to assess the possible role of western boundary reflections, we projected the FSU and SSM/I western Pacific wind stress in terms of Kelvin forcing. As discussed by *Busalacchi et al.* [1993], the SSM/I wind product has a better time/space resolution in the western Pacific than other products relying on ship and buoy wind observations. Figure 6 shows the FSU and SSM/I Kelvin forcing averaged within 130°E–160°E, together with Kelvin contribution to ZCA at the equator and 160°E (the western limit of our domain). Interestingly, time series of Kelvin forcing and Kelvin contribution to ZCA present a good correspondence, propounding that wind forcing was the main trigger of Kelvin waves propagating from the western toward the central Pacific. Once again, this tends to controvert the possible role of Rossby reflection at the western boundary regarding the termination of the 1986–1987 El Niño.

Given the sign of Kelvin and Rossby contributions to ZCA at 160°E (discussed above from Plates 3b and 3c) and the close relation between Kelvin forcing and Kelvin contribution to ZCA in the western Pacific (discussed above from Figure 6), our observational study does not plead in favor of the delayed action oscillator mechanism, at least during the specific 1986–1989 ENSO cycle. The schematic scenario proposed by Picaut and Delcroix (submitted manuscript, 1994), in which a downwelling Rossby wave originating from the eastern Pacific was the reason for the 1986–1987 El Niño to turn to the 1988–1989 La Niña, gives credit to this conclusion. Notwithstanding, the importance of western boundary reflections, i.e., the relevance of the delayed action oscillator mechanism, is still debated in modeling studies. As a matter of fact, sensitivity tests conducted on idealized ENSO cycles show that replacing the solid western boundary with an open boundary (i.e., allowing no reflection) either annihilates [e.g., *Battisti*, 1988] or does not change [*Yang and O'Brien*, 1993] the period of simulated ENSO. As noted by *Battisti* [1988], only a thorough obser-

vational study in the western equatorial Pacific might decide whether or not reflection is a potentially important mechanism. We can expect that the unprecedented high-quality altimeter data gathered by the ongoing TOPEX/POSEIDON mission will help to refine and extend our analysis to the 1992–1993 ENSO.

Appendix

A brief review of the linear theory of equatorial waves is presented to establish the framework of our analysis. Considering a 1 1/2-layer, reduced gravity model on an equatorial β plane, scaled by a horizontal length scale $L = (c/\beta)^{1/2}$ and a timescale $T = 1/(\beta c)^{1/2}$ with $c = (g'H)^{1/2}$, where g' is the reduced gravity and H is the mean thermocline depth, the long-wave, low-frequency, shallow water equations are written as:

$$\begin{aligned} u_t - yv + h_x &= F \\ yu + h_y &= G \\ h_t + u_x + v_y &= 0 \end{aligned} \tag{A1}$$

where $x(y)$ is the zonal (meridional) distance; $u(v)$ is the zonal (meridional) velocity component; h, the upper layer thickness, F, G, 0, the components of the scaled forcing function, and subscripts denote differentiation. *Cane and Sarachik* [1976] have shown that the homogeneous equations (A1) with variables proportional to exp $[i(kx - \omega t)]$, where k and ω are the zonal wavenumber component and frequency, respectively, may be reduced to a single equation in v

$$v_{yy} + \left(\omega^2 - \frac{k}{\omega} - k^2 - y^2\right)v = 0. \tag{A2}$$

The dispersion relation

$$\omega^2 - \frac{k}{\omega} - k^2 = 2n + 1 \tag{A3}$$

results from the boundary solution that $v \to 0$ when $y \to \pm\infty$, and the corresponding eigenfunctions are

$$\psi_n(y) = (2^n n! \pi^{1/2})^{-1/2} e^{-y^2/2} H_n(y) \tag{A4}$$

where $n > 0$ is an integer meridional mode number and $H_n(y)$ are the Hermite polynomials ($H_1 = y$; $H_2 = 4y^2 - 2$, etc. . . .). One additional solution $v = 0$ exists in (A2) for which $\omega = k$ and n is set to -1 in extrapolating (A3).

The Kelvin ($n = -1$) and Rossby ($n > 1$) solutions form a complete and orthogonal system for the shallow water equations [*Cane and Sarachik*, 1976]. Following *Cane and Sarachik* [1981], we define an inner product [**A**, **B**] together with normalized Kelvin ($\mathbf{M}_k$) and Rossby ($\mathbf{R}_n$) vector functions as

$$[\mathbf{A}, \mathbf{B}] = \int_{-\infty}^{+\infty} (A_u B_u + A_h B_h)\, dy \tag{A5}$$

$$\mathbf{A} = \begin{bmatrix} A_u \\ A_h \end{bmatrix} \qquad \mathbf{B} = \begin{bmatrix} B_u \\ B_h \end{bmatrix}$$

$$\mathbf{M}_k = 2^{-1/2} \begin{bmatrix} \psi_0(y) \\ \psi_0(y) \end{bmatrix} \tag{A6a}$$

$$\mathbf{R}_n = 2^{-3/2} \begin{bmatrix} (n+1)^{-1/2}\psi_{n+1}(y) - n^{-1/2}\psi_{n-1}(y) \\ (n+1)^{-1/2}\psi_{n+1}(y) + n^{-1/2}\psi_{n-1}(y) \end{bmatrix} \tag{A6b}$$

where the first and second component in $\mathbf{M}_k$ and $\mathbf{R}_n$ refer to u and h, respectively. The orthogonal vector functions $\mathbf{M}_k$ and $\mathbf{R}_n$ have their u velocities in geostrophic balance and satisfy the normalization conditions:

$$[\mathbf{M}_k, \mathbf{M}_k] = 1 \qquad [\mathbf{R}_n, \mathbf{R}_m] = \frac{2n+1}{4n(n+1)}\,\delta_{n,m} \tag{A7}$$

with

$$\delta_{n,m} = 1 \qquad n = m$$

$$\delta_{n,m} = 0 \qquad n \neq m$$

Given the orthogonality and completeness of the Kelvin and Rossby vectors, any vector **G** can be written as:

$$\mathbf{G} = \alpha_k \mathbf{M}_k + \sum_{n=0}^{\infty} \alpha_{r,n} \mathbf{R}_n \tag{A8}$$

with

$$\alpha_k = \frac{[\mathbf{G}, \mathbf{M}_k]}{[\mathbf{M}_k, \mathbf{M}_k]} \qquad \alpha_{r,n} = \frac{[\mathbf{G}, \mathbf{R}_n]}{[\mathbf{R}_n, \mathbf{R}_n]} \tag{A9}$$

Defining a "Geosat vector" **G** as

$$\mathbf{G} = \begin{bmatrix} u'_g \\ h'_g \end{bmatrix} \tag{A10}$$

where u'_g and h'_g are the scaled components ($u'_g = u/c$; $h'_g = gh/c$), this theoretical approach is applied to the Geosat-derived sea level and surface zonal velocity. Using (A4) and (A6), the normalized Kelvin ($\mathbf{M}_k$) and first three Rossby ($\mathbf{R}_1$, $\mathbf{R}_2$, $\mathbf{R}_3$) vector functions become

$$\begin{aligned} \mathbf{M}_k &= 2^{-1/2}\pi^{-1/4} e^{-y^2/2} \begin{bmatrix} 1 \\ 1 \end{bmatrix} \\ \mathbf{R}_1 &= 2^{-3/2}\pi^{-1/4} e^{-y^2/2} \begin{bmatrix} y^2 - 3/2 \\ y^2 + 1/2 \end{bmatrix} \\ \mathbf{R}_2 &= 2^{-1/2}\pi^{-1/4} e^{-y^2/2} \begin{bmatrix} y^3/3 - y \\ y^3/3 \end{bmatrix} \\ \mathbf{R}_3 &= [4(3)^{1/2}]^{-1}\pi^{-1/4} e^{-y^2/2} \begin{bmatrix} y^4 - 5y^2 + 7/4 \\ y^4 - y^2 - 1/4 \end{bmatrix} \end{aligned} \tag{A11}$$

These components are shown in Figure A1. The projection of the Kelvin and first three Rossby modes to the scaled surface current and sea level is then derived from (A8) and (A9).

In a similar way the forcing function, defined as the scaled wind stress vectors $\boldsymbol{\tau}' = \boldsymbol{\tau}/\rho H$, is projected onto the equatorial modes. In general, the Rossby modes are forced by both components of the wind stress. However, it is only the zonal wind stress that matters for the long-wave approximation. From the forced shallow water equations the pro-

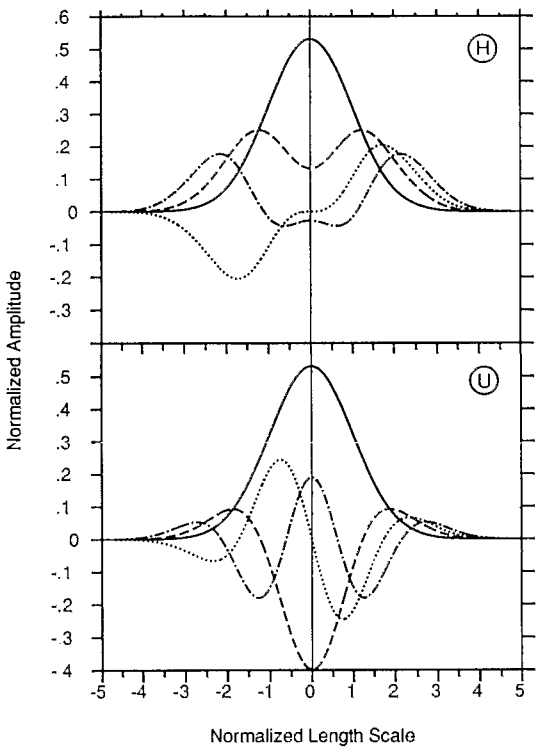

Figure A1. Meridional distributions of the normalized Kelvin modes (solid line), first symmetric Rossby modes (dashed line), first antisymmetric Rossby modes (dotted line), and second symmetric Rossby modes (dash-dotted line). The length scale is normalized by $L = (c/\beta)^{1/2}$, meaning that 1 unit is equivalent to 3.15° latitude using c = 2.8 m/s. (top) H is for sea level, and (bottom) U is for zonal current.

jection of the zonal wind anomalies onto the Kelvin and first symmetric Rossby modes in the meridionally unbounded case are written as

$$F_k = 2^{-1/2} \int_{-\infty}^{+\infty} \tau'^x \psi_0(y)\, dy \qquad \text{(A12a)}$$

$$F_{R_1} = \frac{1}{3} \int_{-\infty}^{+\infty} \tau'^x \{\psi_2(y) - [2^{1/2}\psi_0(y)]\}\, dy \qquad \text{(A12b)}$$

The integrals in (A9) and (A12) are calculated numerically using the trapezoidal rule. Combined with the fact that the FSU wind field is averaged over 1 month, it is worth noting that the numerical calculation underestimates (A12), given the 2° latitude coarse meridional resolution of this wind field. Sensitivity studies using analytical test functions show that for the 2° latitude spacing the degradation of integrals tantamount to (A12) is of the order of 25% [*Gill and Bigg*, 1985]. The meridional ocean boundaries y are defined between 30°N and 30°S when they exist. As expected from Figure A1, confining (A9) and (A12) between y = 10°N and 10°S does not change the result significantly, as long as only first baroclinic Kelvin and mode 1–3 Rossby waves are concerned. Given the presence of continents, calculation of (A9) and (A12b) thus zonally restrict our domain to 160°E–90°W. Note, however, that (A12a) can be estimated west of 160°E where meridional boundaries exist near the equator [*Cane and Sarachik*, 1979]. Besides, (A9) and (A12) are calculated with a constant phase speed c = 2.8 m/s everywhere, although the real hydrographic structure of the tropical Pacific indicates zonal and meridional variation in the first baroclinic mode speed [*Picaut and Sombardier*, 1993]. Choosing different phase speed $c \pm 10\%$ does not affect our main conclusions.

Acknowledgments. The bulk of this work relies on the Geosat geophysical data records (GDR) prepared and distributed on six CD ROMs by the U.S. National Oceanic and Atmospheric Administration. Fruitful and informative electronic mail with R. E. Cheney has clarified numerous questions dealing with GDR and Geosat data processing. Programming support at the early stage of this work was given by J. P. Porte. Part of the Geosat validation study was made possible using in situ TOGA sea level measurements made available to us by K. Wyrtki and G. Mitchum. The TOGA-TAO measurements of temperature, salinity, and equatorial current, provided by M. McPhaden and coworkers, were instrumental in the validation study. The Florida State University wind field data set was supplied by J. O'Brien and coworkers. The SSM/I wind product was provided by E. Hackert. We had copious helpful discussions with J. Picaut and fruitful comments from Y. duPenhoat and A. Busalacchi. Referenced modeling studies inspired us to focus within the equatorial band, trying to unravel the 1986–1989 ENSO in terms of equatorial Kelvin and first symmetric Rossby modes only. Support for this work was provided by the Programme National de Télédétection Spatiale. All these direct and indirect contributions are gratefully acknowledged.

References

Arnault, S., and C. Périgaud, Altimetry and models in the tropical oceans: A review, *Oceanol. Acta, 15*, 411–430, 1992.

Battisti, D., Dynamics and thermodynamics of a warming event in a coupled tropical atmosphere-ocean model, *J. Atmos. Sci., 45*, 2889–2919, 1988.

Bigg, G., and J. Blundell, The equatorial Pacific prior to and during El Niño of 1982/83—A normal mode model view, *Q. J. R. Meteorol. Soc., 115*, 1039–1069, 1989.

Busalacchi, A., and M. Cane, Hindcasts of sea level variations during the 1982–83 El Niño, *J. Phys. Oceanogr., 15*, 213–221, 1985.

Busalacchi, A., and J. O'Brien, Interannual variability of the equatorial Pacific in the 1960s, *J. Geophys. Res., 86*, 10,901–10,907, 1981.

Busalacchi, A., R. Atlas, and E. Hackert, Comparison of special sensor microwave imager vector wind stress with model-derived and subjective products for the tropical Pacific, *J. Geophys. Res., 98*, 6961–6977, 1993.

Cane, M., and E. Sarachik, Forced baroclinic ocean motions, I, The linear equatorial unbounded case, *J. Mar. Res., 34*, 629–665, 1976.

Cane, M., and E. Sarachik, Forced baroclinic ocean motions, III, The linear equatorial basin case, *J. Mar. Res., 37*, 355–398, 1979.

Cane, M., and E. Sarachik, The response of a linear baroclinic equatorial ocean to periodic forcing, *J. Mar. Res., 39*, 651–693, 1981.

Cane, M., S. Zebiak, and S. Dolan, Experimental forecasts of El Niño, *Nature, 321*, 827–832, 1986.

Chao, Y., D. Halpern, and C. Périgaud, Sea surface height variability during 1986–1988 in the tropical Pacific ocean, *J. Geophys. Res., 98*, 6947–6959, 1993.

Cheney, R., B. Douglas, R. Agreen, L. Miller, D. Porter, and N. Doyle, GEOSAT altimeter GDR, user handbook, 29 pp., Natl. Ocean Surv., Natl. Oceanic and Atmos. Admin., Silver Spring, Md., 1987.

Cheney, B., B. Douglas, and L. Miller, Evaluation of Geosat altimeter data with application to tropical Pacific sea level variability, *J. Geophys. Res., 94*, 4737–4747, 1989.

Cheney, R., N. Doyle, B. Douglas, R. Agreen, L. Miller, E. Timmerman, and D. McAdoo, The complete GEOSAT altimeter

GDR handbook, 79 pp., Natl. Ocean Surv., Natl. Oceanic and Atmos. Admin., Silver Spring, Md., 1991.

Delcroix, T., Seasonal and interannual variability of sea-surface temperatures in the tropical Pacific, 1969–1991, *Deep Sea Res., Part I, 40*, 2217–2228, 1993.

Delcroix, T., G. Eldin, and C. Hénin, Upper ocean water masses and transports in the western tropical Pacific (165°E), *J. Phys. Oceanogr., 17*, 2248–2262, 1987.

Delcroix, T., J. Picaut, and G. Eldin, Equatorial Kelvin and Rossby waves evidenced in the Pacific Ocean through Geosat sea level and surface current anomalies, *J. Geophys. Res., 96*, 3249–3262, 1991.

Delcroix, T., G. Eldin, M. H. Radenac, J. Toole, and E. Firing, Variations of the western equatorial Pacific Ocean, 1986–1988, *J. Geophys. Res., 97*, 5423–5445, 1992.

duPenhoat, Y., T. Delcroix, and J. Picaut, Interpretation of Kelvin/Rossby waves in the equatorial Pacific from model-GEOSAT data intercomparison during the 1986–1987 El Niño, *Oceanol. Acta, 15*, 545–554, 1992.

Emery, W., G. Born, D. Baldwin, and C. Norris, Satellite-derived water vapor corrections for Geosat altimetry, *J. Geophys. Res., 95*, 2953–2964, 1990.

Freitag, H., M. McPhaden, and A. Shepherd, Equatorial current and temperature data: 108°W to 110°W, October 1979 to November 1983, *NOAA Data Rep. ERL PMEL-17*, 99 pp., Pac. Mar. Environ. Lab., Seattle, Wash., 1987.

Fu, L., J. Vasquez, and C. Périgaud, Fitting dynamic models to the Geosat sea level observations in the tropical Pacific Ocean, I, A free wave model, *J. Phys. Oceanogr., 21*, 798–809, 1991.

Fu, L., I. Fukumori, and R. Miller, Fitting dynamic models to the Geosat sea level observations in the tropical Pacific Ocean, II, A linear, wind-driven model, *J. Phys. Oceanogr., 23*, 2162–2181, 1993.

Gill, A., Changes in thermal structure of the equatorial Pacific during the 1972 El Niño, as revealed by bathythermograph observations, *J. Phys. Oceanogr., 12*, 1373–1387, 1982.

Gill, A., An estimation of sea-level and surface-current anomalies during the 1972 El Niño and consequent thermal effects, *J. Phys. Oceanogr., 13*, 586–606, 1983.

Gill, A., and G. Bigg, Some preliminary results of a search for equatorial long waves, *Trop. Ocean Atmos. Newsl., 31*, 2–4, 1985.

Goldenberg, S., and J. O'Brien, Time and space variability of tropical wind stress, *Mon. Weather Rev., 109*, 1190–1207, 1981.

Haines, B., G. Born, G. Rosborough, J. Marsh, and R. Williamson, Precise orbit computation for the Geosat exact repeat mission, *J. Geophys. Res., 95*, 2871–2886, 1990.

Hansen, D., and C. Paul, Genesis and effects of long waves in the equatorial Pacific, *J. Geophys. Res., 89*, 10,431–10,440, 1984.

Kessler, W., Observations of long Rossby waves in the northern tropical Pacific, *J. Geophys. Res., 95*, 5183–5219, 1990.

Levitus, S., Climatological atlas of the world ocean, *NOAA Prof. Pap. 13*, 173 pp., U.S. Govt. Print. Office, Washington, D. C., 1982.

Marsh, J., et al., The GEM-T2 gravitational model, *J. Geophys. Res., 95*, 22,043–22,071, 1990.

Matsuno, T., Quasi-geostrophic motions in the equatorial area, *J. Meteorol. Soc. Jpn., 44*, 25–42, 1966.

McPhaden, M., and S. Hayes, Variability in the eastern equatorial Pacific ocean during 1986–1988, *J. Geophys. Res., 95*, 13,195–13,208, 1990.

McPhaden, M., and J. Picaut, El Niño-Southern Oscillation displacements of the western equatorial Pacific warm pool, *Science, 250*, 1385–1388, 1990.

McPhaden, M., S. Hayes, L. Mangum, and J. Toole, Variability in the western equatorial Pacific Ocean during the 1986–87 El Niño/Southern Oscillation Event, *J. Phys. Oceanogr., 20*, 190–208, 1990.

Miller, L., R. Cheney, and B. Douglas, GEOSAT altimeter observations of Kelvin waves and the 1986–1987 El Niño, *Science, 239*, 52–54, 1988.

Moore, D., Planetary-gravity waves in an equatorial ocean, Ph.D. thesis, 207 pp., Harvard Univ., Cambridge, Mass., 1968.

Philander, G., *El Niño, La Niña, and the Southern Oscillation*, 293 pp., Academic, San Diego, Calif., 1990.

Picaut, J., and L. Sombardier, Influence of density stratification and bottom depth on vertical mode structure functions in the tropical Pacific, *J. Geophys. Res., 98*, 14,727–14,737, 1993.

Picaut, J., and R. Tournier, Monitoring the 1979–1985 equatorial Pacific current transports with bathythermograph data, *J. Geophys. Res., 96*, 3263–3277, 1991.

Picaut, J., A. Busalacchi, M. McPhaden, and B. Camusat, Validation of the geostrophic method for estimating zonal currents at the equator from Geosat altimeter data, *J. Geophys. Res., 95*, 3015–3024, 1990.

Tournier, R., Variabilité de la structure thermique et des courants à l'ouest et au centre de l'océan Pacifique tropical, thèse, 154 pp., Univ. Pierre et Marie Curie, Paris, 1989.

Wakata, Y., and E. Sarachik, On the role of equatorial ocean modes in the ENSO cycle, *J. Phys. Oceanogr., 21*, 434–443, 1991.

Wentz, F., User's manual for the collocated GEOSAT SSMI tape, 16 pp., Remote Sens. Syst., Santa Rosa, Calif., 1989.

White, W. B., and C. K. Tai, Reflection of interannual Rossby waves at the maritime western boundary of the tropical Pacific, *J. Geophys. Res., 97*, 14,305–14,322, 1992.

Wyrtki, K., El Niño—The dynamic response of the equatorial Pacific ocean to atmospheric forcing, *J. Phys. Oceanogr., 5*, 572–584, 1975.

Wyrtki, K., et al., The Pacific island sea level network, *Contrib. 88-0137, Data Rep. 002*, Joint Inst. for Mar. and Atmos. Res., Honolulu, Hawaii, 1988.

Yang, J., and J. O'Brien, A coupled atmosphere-ocean model in the tropics with different thermocline profiles, *J. Clim., 6*, 1027–1040, 1993.

Zlotnicki, V., Sea level differences across the Gulf Stream and Kuroshio extension, *J. Phys. Oceanogr., 21*, 599–609, 1991.

J.-P. Boulanger, ORSTOM/LOYDC, Université Pierre et Marie Curie, 4, place Jussieu, Paris, France.

T. Delcroix and F. Masia, Groupe SURTROPAC, ORSTOM, B. P. A5, Noumea, New Caledonia.

C. Menkes, Universities Space Research Association, Goddard Space Flight Center, Greenbelt, MD 20771.

(Received February 10, 1994; revised June 14, 1994; accepted August 15, 1994.)